Initial Human PET Studies of Metabotropic Glutamate Receptor Type 1 Ligand ^{11}C-ITMM

Jun Toyohara[1], Muneyuki Sakata[1], Keiichi Oda[1], Kenji Ishii[1], Kimiteru Ito[1,2], Mikio Hiura[1,3], Masayuki Fujinaga[4], Tomoteru Yamasaki[4], Ming Rong Zhang[4], and Kiichi Ishiwata[1]

[1]Research Team for Neuroimaging, Tokyo Metropolitan Institute of Gerontology, Tokyo, Japan; [2]Department of Radiology, National Center for Neurology and Psychiatry, Tokyo, Japan; [3]Faculty of Sports and Health Studies, Hosei University, Tokyo, Japan; and [4]Molecular Imaging Center, National Institute of Radiological Sciences, Chiba, Japan

N-[4-[6-(isopropylamino)pyrimidin-4-yl]-1,3-thiazol-2-yl]-4-^{11}C-methoxy-*N*-methylbenzamide (^{11}C-ITMM) is a potential radioligand for mapping metabotropic glutamate receptor type 1 (mGluR1) in the brain by PET. The present study was performed to determine the safety, distribution, radiation dosimetry, and initial brain imaging of ^{11}C-ITMM in healthy human subjects. **Methods:** The multiorgan biodistribution and radiation dosimetry of ^{11}C-ITMM were assessed in 3 healthy human subjects, who underwent 2-h whole-body PET scans. Radiation dosimetry was estimated from the normalized number of disintegrations of source organs using the OLINDA/EXM program. Five healthy human subjects underwent 90-min dynamic ^{11}C-ITMM scans of brain regions with arterial blood sampling. For anatomic coregistration, T1-weighted MR imaging was performed. Metabolites in plasma and urine samples were analyzed by high-performance liquid chromatography. ^{11}C-ITMM uptake was assessed quantitatively using a 2-tissue-compartment model. **Results:** There were no serious adverse events in any of the subjects throughout the study period. ^{11}C-ITMM PET demonstrated high uptake in the urinary bladder and gallbladder, indicating both urinary and fecal excretion of radioactivity. The absorbed dose (μGy/MBq) was highest in the urinary bladder wall (13.2 ± 3.5), small intestine (9.8 ± 1.7), and liver (9.1 ± 2.0). The estimated effective dose for ^{11}C-ITMM was 4.6 ± 0.3 μSv/MBq. ^{11}C-ITMM showed a gradual increase of radioactivity in the cerebellar cortex. The total distribution volume in the brain regions ranged from 2.61 ± 0.30 (cerebellar cortex) to 0.52 ± 0.17 (pons), and the rank order of the corresponding total distribution volume of ^{11}C-ITMM was cerebellar cortex > thalamus > frontal cortex > striatum ≈ pons, which was consistent with the known distribution of mGluR1 in the primate brain. The rate of ^{11}C-ITMM metabolism in plasma was moderate: at 60 min after injection, 62.2% ± 8.2% of the radioactivity in plasma was intact parent compound. **Conclusion:** The initial findings of the present study indicated that ^{11}C-ITMM PET is feasible for imaging of mGluR1 in the brain. The low effective dose will permit serial examinations in the same subjects.

Key Words: ITMM; radiation dosimetry; human brain; metabotropic glutamate receptor

J Nucl Med 2013; 54:1302–1307
DOI: 10.2967/jnumed.113.119891

Glutamate is an excitatory neurotransmitter in the central nervous system (CNS) and is involved in many pathologic conditions of the CNS. Glutamate receptors are divided into metabotropic (mGluRs) and ionotropic types based on their biologic functions and molecular structures (*1*). The mGluRs are classified into 3 groups, including 8 subtypes, according to sequence homology, G-protein–coupling mechanisms, and pharmacologic activity (*2,3*). The mGluR subtype 1 (mGluR1) is one of the group I receptors localized postsynaptically in the cerebellar Purkinje cells, striatonigral and striatopallidal projection neurons, and striatal interneurons (*4,5*). The distribution of mGluR1 in the rodent brain has been identified by in vitro autoradiography and immunohistochemistry (*6,7*). These studies demonstrated a wide distribution of mGluR1 in the rat brain, with a high level of expression in the cerebellum; moderate or low levels in the thalamus, striatum, and cerebral cortex; and a very low level in the brain stem. Several studies have demonstrated that mGluR1 is involved in spatial and associative learning (*8*) and in synaptic plasticity regulation in the hippocampus and cerebellum (*9*). It has been suggested that mGluR1 may be a drug target for the treatment of diseases, such as stroke, epilepsy, pain, cerebellar ataxia, neurodegenerative disorders, anxiety, and mood disorders (*9–11*). Therefore, in vivo imaging of mGluR1 may provide crucial information about its functions in the living human brain under healthy and pathologic conditions and facilitate the development of CNS drugs targeting mGluR1. Several groups have developed radiotracers for selective imaging of mGluR1 in the human brain by PET (*12–20*). Despite these efforts, there have been no clinical studies using radioligands for mGluR1 in the human brain. Conversely, 3 mGluR subtype 5 (mGluR5) PET ligands (i.e., 3-(6-methyl-pyridin-2-ylethynyl)-cyclohex-2-enone-*O*-^{11}C-methyl-oxime [^{11}C-ABP688], 3-fluoro-5-[2-[2-^{18}F-(fluoromethyl)thiazol-4-yl]ethynyl]benzonitrile [^{18}F-SP203], and ^{18}F-3-fluoro-5-[(pyridine-3-yl)ethynyl]benzonitrile [^{18}F-FPEB]) have entered clinical trials (*21*). Recently, Fujinaga et al. developed *N*-[4-[6-(isopropylamino)pyrimidin-4-yl]-1,3-thiazol-2-yl]-4-^{11}C-methoxy-*N*-methylbenzamide (^{11}C-ITMM) as a novel PET ligand for mGluR1 in the rodent brain (*22*). An in vitro binding study showed high affinity and selectivity of ^{11}C-ITMM to mGluR1 (*Ki* = 12.6 nM; mGluR5/mGluR1, >306). ^{11}C-ITMM was found to have less activity for 28 standard receptor binding sites, including major classes of neurotransmitter receptors, uptake systems, and ion channels (*23*). ^{11}C-ITMM distributions in the rat brain measured by in vitro autoradiography and small-animal PET were consistent with the regional distribution of mGluR1. In

Received Jan. 14, 2013; revision accepted Mar. 28, 2013.
For correspondence or reprints contact: Jun Toyohara, Research Team for Neuroimaging, Tokyo Metropolitan Institute of Gerontology, 1-1 Naka-cho, Itabashi-ku, Tokyo 173-0022, Japan.
E-mail: toyohara@pet.tmig.or.jp
Published online Jun. 26, 2013.
COPYRIGHT © 2013 by the Society of Nuclear Medicine and Molecular Imaging, Inc.

contrast, only a very low and uniform distribution of radioactivity was found in the mGluR1 knockout mouse brain. Moreover, brain uptake of ^{11}C-ITMM was selectively blocked by pretreatment with the mGluR1-selective ligand JNJ16259685 (*24*) and carrier loading.

Recently, we conducted preclinical safety and radiation dosimetry studies of ^{11}C-ITMM injection for human use (*23*). The results indicated that ^{11}C-ITMM injection has sufficient quality for clinical use. The radiation-absorbed dose was slightly higher in the urinary bladder walls than in other organs studied but was nonetheless low enough for clinical use. The absence of any abnormalities in rats in the acute toxicity test and the absence of mutagenicity of ITMM together demonstrated the clinical suitability of ^{11}C-ITMM for use in PET studies in humans. These findings prompted us to undertake an initial evaluation of ^{11}C-ITMM in human subjects. Here, we report the safety, radiation dosimetry, and initial brain imaging of ^{11}C-ITMM in human subjects.

MATERIALS AND METHODS

General

ITMM and its precursor, *N*-[4-[6-(isopropylamino)pyrimidin-4-yl]-1,3-thiazol-2-yl]-4-hydroxy-*N*-methylbenzamide, were prepared by the method described previously (*22*). All chemical reagents were obtained from commercial sources.

Preparation of ^{11}C-ITMM

Methylation of the *O*-desmethyl precursor with ^{11}C-methyl triflate was performed by the previously described procedure (*23*).

Subjects

Eight healthy male volunteers, aged 21−27 y (mean age ± SD, 22.8 ± 1.9 y), were enrolled in this study. Five of the 8 subjects were recruited into the dynamic brain PET study. The subjects weighed 60.2–76.0 kg (mean weight ± SD, 67.5 ± 6.0 kg). For anatomic coregistration, a 3-dimensional spoiled gradient-echo (repetition time, 21 ms; echo time, 6 ms; matrix, 56 × 256 × 125 voxels) T1-weighted whole-brain image was acquired for each subject on a 1.5-T Signa system (GE Healthcare). These subjects were also included in the safety monitoring of ^{11}C-ITMM. The other 3 subjects participated in the whole-body distribution study. The subjects weighed 49.0–66.3 kg (mean weight ± SD, 55.8 ± 9.2 kg). All subjects were free of somatic and neuropsychiatric illnesses, according to medical history and findings of physical examination. The study protocol was approved by our Institutional Review Board. Written informed consent was obtained from each subject after the procedures had been fully explained.

Safety Monitoring

Safety data were collected after administration of ^{11}C-ITMM and throughout the follow-up period of 1 wk in 5 subjects. Safety monitoring included the recording of adverse events, changes in vital signs, physical examination, electrocardiogram, and laboratory parameters (serum biochemistry and hematology analysis). Vital signs—including blood pressure, temperature, and respiratory rate—were monitored and recorded closely during ^{11}C-ITMM imaging procedures at baseline; during ^{11}C-ITMM injection; during PET scanning at 20, 40, and 60 min; and then within approximately 1 h after PET scanning. The electrocardiogram was recorded continuously starting before the ^{11}C-ITMM injection and throughout the whole imaging procedure. Blood samples were obtained at baseline and 1 wk after radioligand administration in all subjects. The following blood assays were performed: sodium, potassium, chloride, calcium, and glucose levels; hepatic function assays (aspartate aminotransferase, alanine aminotransferase, alkaline phosphatase, lactate dehydrogenase, cholinesterase, and total protein); creatinine and blood urea nitrogen; amylase and creatine kinase; lipid metabolism (total cholesterol and triglyceride); and hematologic evaluation consisting of a complete blood count, including red blood cell count, hematocrit, hemoglobin, white blood cell count, differential leukocyte count, and platelet count.

Whole-Body Imaging

The protocol for investigating radiation dosimetry in human subjects using whole-body imaging was essentially the same as that reported previously (*25*). Whole-body PET scans were obtained using an SET-2400W scanner (Shimadzu) in 2-dimensional mode. This scanner has an axial field of view of 20 cm and acquires 63 slices at a center-to-center interval of 3.125 mm (*26*). Before the injection of ^{11}C-ITMM, the subjects were asked to void their bladders. Whole-body emission scans were obtained with 7 frames (~125 min in total) from 1 min after the intravenous bolus injection of 634 ± 55 MBq (6.9–13.8 nmol) of ^{11}C-ITMM. Each frame covered the body from the head to the urinary bladder and consisted of 5 bed positions. The duration of scanning at each bed position was increased to compensate for the short half-life of ^{11}C: 120 s/bed positions for 1–3 frames, 240 s/bed positions for 4–6 frames, and 360 s/bed positions for the last frame. At the last frame, transmission data with a rotating ^{68}Ge/^{68}Ga line source to correct for attenuation were acquired simultaneously (*27*). The sum of intervals for the moving bed was ≈90 s/frame. After the dynamic PET procedure, the subjects were asked to urinate again, and radioactivity of the urine was measured using a radioisotope calibrator (CRC-712; Capintec). Images were reconstructed with ordered-subset expectation maximization, followed by the application of a gaussian postprocessing filter of 6 mm in full width at half maximum. The resulting images were 128 × 128 × 25 voxels for each bed position (voxel size, 4 × 4 × 6.25 mm). Regions of interest (ROIs) were placed over 15 organs that could be identified: brain, thyroid, thymus, lungs, heart wall, liver, spleen, stomach, pancreas, gallbladder, adrenals, bone marrow (thoracic and lumbar vertebrae), small intestine, kidneys, and urinary bladder. The decay-uncorrected and decay-corrected time–activity curves of organs were calculated as the percentage injected dose per organ or as a standardized uptake value (SUV): (activity/mL tissue)/(injected activity/g body weight). The normalized number of disintegrations (MBq-h/MBq administered) for each source organ is equal to the area under the time course curve multiplied by the volume of the organ ROI. The volume of bone marrow, in which only part of the organ could be measured, was substituted by the volume, which was calculated from the mass of red marrow in the adult male phantom (1.12 kg for 73.7 kg of body weight) adjusted by the subject's body weight and 1 g/mL as the specific gravity (*28*). For organs that were measured in 2 split images of different bed positions, the number of disintegrations was calculated independently for each bed position and aggregated. The area under the time course curve was calculated by summing the area from time 0 to the endpoint of the scan and the area from the endpoint of the scan to infinity. The former area was calculated by trapezoidal integration. The latter area was calculated by integration of a monoexponential curve passing through the final 2 scan points.

The absorbed dose in 25 target organs of the adult male phantom was estimated from the normalized number of disintegrations of source organs by implementing the Radiation Dose Assessment Resource method using OLINDA/EXM (Vanderbilt University) (*29*). The effective dose was also calculated by OLINDA/EXM using the methodology described in International Commission on Radiological Protection Publication 60 (*30*).

Brain PET Scanning

PET scans with ^{11}C-ITMM were obtained using an SET-2400W scanner. After transmission scanning with a rotating ^{68}Ge/^{68}Ga line

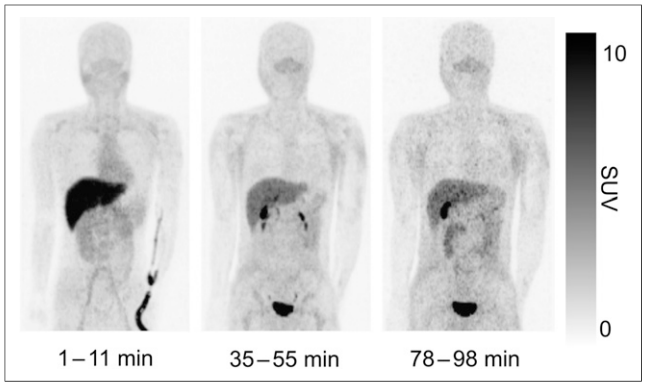

FIGURE 1. Representative whole-body decay-corrected maximum-intensity-projection images of ^{11}C-ITMM. Images were obtained at 1–11, 35–55, and 78–98 min after intravenous injection of ^{11}C-ITMM into healthy male subject.

source to correct for attenuation, ^{11}C-ITMM (511–628 MBq/5.5–12.0 nmol) was injected intravenously for 1 min into each subject, and then dynamic PET scanning (90 min) with 2-dimensional acquisition (20 s × 3, 30 s × 3, 60 s × 5, 150 s × 5, and 300 s × 14 frames) was performed. After the dynamic scan, urine was recovered from the subjects. Arterial blood (0.5 mL each) was sampled at 10, 20, 30, 40, 50, 60, 70, 80, 90, 100, 110, 120, 135, 150, and 180 s and at 5, 7, 10, 15, 20, 30, 40, 50, 60, 75, and 90 min. The whole blood and separated plasma were weighed, and radioactivity was measured with a NaI (Tl) well scintillation counter. To analyze the labeled metabolites, 1.5 mL of additional blood was obtained at 3, 10, 20, 30, 40, and 60 min. Unaltered ^{11}C-ITMM in the plasma was analyzed by high-performance liquid chromatography (HPLC), and the metabolite-corrected time–activity curve of plasma was obtained as described below.

Tomographic images were reconstructed using a filtered back-projection method with a cutoff frequency of 1.25 cycles/cm and an order of 2. The data were collected in a 128 × 128 × 31 matrix, and the voxel size was 2 × 2 × 6.25 mm. Partially overlapping circular ROIs 10 mm in diameter were placed on the frontal cortex, striatum, thalamus, pons, and cerebellar cortex with reference to the coregistered MR images. Time–activity curves for these ROIs were calculated as Bq/mL or as SUV. Using the time–activity curves of tissues and the metabolite-corrected time–activity curve of plasma, we evaluated the total distribution volume ($V_T = K_1/k_2 \times (1 + k_3/k_4)$) for ^{11}C-ITMM using the 1- and 2-tissue-compartment models. The goodness of fit by the 2-model analysis was evaluated using Akaike's information criterion (AIC). For monitoring of the averaged distribution of ^{11}C-ITMM, anatomic normalization with MR imaging using diffeomorphic anatomic registration through exponentiated lie algebra (DARTEL) (*31*) was applied to the static ^{11}C-ITMM PET image (SUV summed for 40–60 min after injection). Briefly, the ^{11}C-ITMM PET images were registered to the respective MR images based on the normalized mutual information measures between the early summed PET image (0–20 min) and the MR images, and the DARTEL flow fields for the anatomic normalization calculated from the MR image were applied to the registered static PET image.

Metabolite Analysis

Metabolites of ^{11}C-ITMM in the plasma sampled at 3, 10, 20, 30, 40, and 60 min and in urine recovered at 101–107 min were analyzed by HPLC. The blood was centrifuged at 7,000*g* for 1 min at 4°C to obtain the plasma, which was denatured with 3 volumes of 67% aqueous acetonitrile in an ice-water bath. The suspension was centrifuged under the same conditions and divided into soluble and precipitable fractions. The precipitate was resuspended in 2 volumes of 50% aqueous acetonitrile, followed by centrifugation. This procedure was repeated twice. Radioactivity in the 3 soluble fractions and precipitates was measured with an auto-γ-counter (Wallac). In this treatment of plasma, <2% of the total radioactivity was left in the final precipitates. The soluble fractions were combined and after centrifugation of the samples as described above, the supernatant was analyzed by HPLC with a radioactivity detector (FLO-ONE 150TR; Packard Instrument). A YMC-Pack ODS-A column (10 × 150 mm; YMC) was used with acetonitrile/50 mM aqueous acetic acid/50 mM aqueous sodium acetate, pH 4.5 (60/20/20, v/v/v), at a flow rate of 4 mL/min. The retention time of ^{11}C-ITMM was 5.8 min. The recovery of the injected radioactivity in the eluate was essentially quantitative.

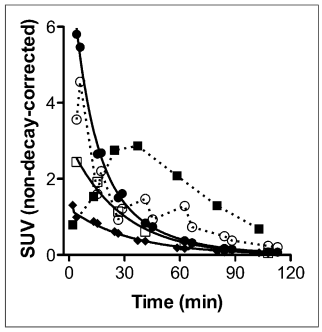

FIGURE 2. Regional non–decay-corrected time–activity curves after intravenous injection of ^{11}C-ITMM into same subject as shown in Figure 1. Time–activity curves of SUVs were obtained with 5 representative source organs: liver (●), gallbladder (○), urinary bladder (■), kidneys (□), and small intestine (♦).

In the case of urine, the sample was applied directly to HPLC.

RESULTS

Safety Monitoring

The mean and SD of the administered mass of ^{11}C-ITMM was 3.3 ± 1.2 μg (range, 2.1–5.3 μg). The mean administered activity was 600 ± 55 MBq (range, 511–691 MBq). The administration of ^{11}C-ITMM was well tolerated by all subjects. There were no adverse or clinically detectable pharmacologic effects in any of the 8 subjects. No clinically important trends indicative of a safety signal were noted for laboratory parameters, vital signs, or electrocardiogram parameters.

Whole-Body Imaging

The representative whole-body distribution of ^{11}C-ITMM is shown in Figure 1. In the first frame, the liver showed the highest uptake of radioactivity, which gradually decreased thereafter. The gallbladder was clearly visible and its radioactivity was secreted into the small intestine, which illustrates the hepatobiliary excretion of ^{11}C radioactivity. The urinary bladder showed a gradual increase in radioactivity, and the highest level of radioactivity uptake was seen in the last frame, which indicated urinary excretion of ^{11}C-ITMM through the kidneys. Figure 2 shows typical non–decay-corrected time–activity curves for the same subject. The radioactivity level showed exponential decay in the liver, kidneys, and small intestine. The time course was more protracted in the gallbladder and urinary bladder. The mean (±SD) radioactivity voided into urine at 133 min ± 1 min (n = 3) was 14.5% ± 1.7% (n = 3) of the injected activity. The normalized number of disintegrations are shown in Supplemental Table 1 (supplemental materials are available online only at http://jnm.snmjournals.org), and the organ absorbed and effective doses are shown in Table 1. The highest absorbed dose was observed in the urinary bladder wall, followed by the small intestine, liver, and heart wall. The mean (±SD) estimated effective dose was 4.6 ± 0.3 μSv/MBq.

TABLE 1
Organ Absorbed Doses

Organ	Absorbed dose (μGy/MBq)
Adrenals	5.9 ± 2.0
Brain	3.6 ± 0.8
Breasts	2.0 ± 0.1
Gallbladder wall	8.0 ± 1.5
Heart wall	8.3 ± 1.2
Kidneys	4.9 ± 2.0
Liver	9.1 ± 2.0
Lower large intestine wall	3.1 ± 0.1
Lungs	4.0 ± 0.3
Muscle	2.4 ± 0.1
Osteogenic cells	4.0 ± 0.1
Ovaries	3.3 ± 0.2
Pancreas	3.6 ± 0.4
Red marrow	3.4 ± 0.1
Skin	1.9 ± 0.1
Small intestine	9.8 ± 1.7
Spleen	2.1 ± 0.2
Stomach wall	8.2 ± 2.9
Testes	2.3 ± 0.1
Thymus	3.9 ± 0.8
Thyroid	3.4 ± 0.5
Upper large intestine wall	3.6 ± 0.2
Urinary bladder wall	13.2 ± 3.5
Uterus	3.5 ± 0.1
Total body	2.8 ± 0.0
Effective dose (μSv/MBq)	4.6 ± 0.3

Data are mean ± SD for healthy male subjects ($n = 3$).

Brain PET Scanning

Figure 3 shows the averaged and anatomically normalized static ^{11}C-ITMM images obtained from 5 healthy human subjects and representative MR imaging results. The tracer was heterogeneously distributed in the brain regions. Figure 4 shows the mean time–activity curves in 5 brain regions after the intravenous injection of ^{11}C-ITMM into a human subject. The radioactivity level in the cerebellar cortex increased continuously over 40 min and then reached a plateau. Radioactivity levels in the other 4 brain regions reached constant levels and then remained steady in the thalamus or decreased gradually in the frontal cortex, striatum, and pons until the end of the scan.

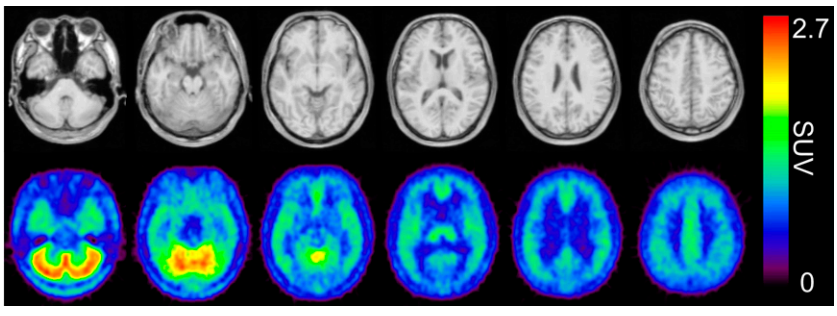

FIGURE 3. Representative MR and mean static images of ^{11}C-ITMM PET obtained from 5 healthy human subjects. Both images were anatomically normalized using diffeomorphic anatomic registration through exponentiated lie algebra (DARTEL). (Upper) MR image. (Lower) Averaged ^{11}C-ITMM PET image (SUV summed 40–60 min; $n = 5$). PET images were smoothed with gaussian filter of 4 mm in full width at half maximum.

The preliminary kinetic analysis of the comparison of AIC (paired t test, $P < 0.05$) in all regions investigated showed that the 2-tissue-compartment model provided significantly better AIC scores than the 1-tissue-compartment model. The rank order of V_T values from the 2-tissue-compartment model ($n = 5$) was cerebellar cortex (2.61 ± 0.30) > thalamus (1.06 ± 0.18) > frontal cortex (0.73 ± 0.09) > striatum (0.53 ± 0.08) ≈ pons (0.52 ± 0.17).

Metabolite Analysis

Plasma radioactivity decreased rapidly after bolus injection (Fig. 5A). The plasma radioactivity concentrations were higher than those of whole blood, suggesting plasma protein binding of ^{11}C-ITMM (Fig. 5B). Two hydrophilic metabolites of ^{11}C-ITMM (2.1 and 3.2 min) appeared in plasma. These radiometabolites were much less lipophilic than the parent (6.2 min). At 60 min after injection, ^{11}C-ITMM was still dominant (Fig. 5A; 62.2% ± 8.2%, $n = 5$). The mean radioactivity voided into urine at 116 ± 14 min (range, 101−133; $n = 8$) was 14.9% ± 4.4% of the injected activity (range, 9.6−17.7; $n = 8$). In urine, 1 major hydrophilic metabolite (2.5 min) was dominant (98.0% ± 1.8%; $n = 3$). The parent radioligand was not detected in voided urine.

DISCUSSION

To our knowledge, no clinically validated PET tracer has been reported for the in vivo imaging of mGluR1. Here, we report the first clinical trials performed with the newly synthesized PET tracer ^{11}C-ITMM for in vivo visualization of mGluR1.

We found ^{11}C-ITMM PET to be safe and well tolerated, with no adverse effects in the 8 subjects included in this study. The radiation-absorbed dose was higher in the urinary bladder wall, small intestine, liver, and heart wall than in the other organs studied but was nonetheless sufficiently low for clinical use. The individual organ and total-body doses associated with ^{11}C-ITMM PET were within the common range of ^{11}C-labeled PET tracers (*32,33*). This lower level of radiation burden is beneficial when obtaining serial PET scans in the same subjects.

Brain PET scans of ^{11}C-ITMM showed the expected distribution patterns of mGluR1 density in the human brain. The localization of human mGluR1 has been demonstrated by in vitro autoradiographic studies with ^{11}C-MMTP (*14*) and ^{18}F-MK-1312 (*15*), 2 selective PET ligands for mGluR1. The highest signal level for mGluR1 was observed in the cerebellar cortex, moderate signals were observed in the thalamus and hippocampus, and the lowest signal levels were detected in the cortical cortex and striatum. Furthermore, the regional distribution of ^{11}C-ITMM was consistent with the known distribution of mGluR1 in the primate brain (*15,17,19*). The individual differences of ^{11}C-ITMM distributions and brain time–activity curves were small in 5 healthy young male subjects. These small individual differences would be advantageous for statistical parametric mapping of mGluR1 density in the brain. To validate this suggestion, further characterizations are needed to determine whether there are sex differences and aging-related alterations of mGluR1 in healthy human subjects.

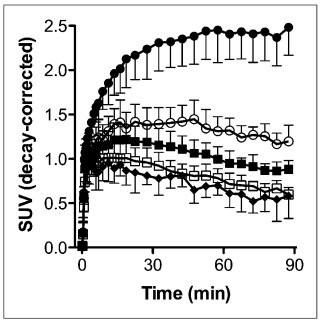

FIGURE 4. Mean decay-corrected time–activity curves of 5 brain regions after intravenous injection of ^{11}C-ITMM into human subject. Radioactivity levels are expressed as SUVs: cerebellar cortex (●), thalamus (○), frontal cortex (■), striatum (□), and pons (♦). Data represent mean ± SD of 5 subjects.

We used a 2-tissue-compartment model and calculated V_T as the outcome measure related to the cerebral mGluR1 density. Logan graphical analysis (*34*) was not appropriate because the slow kinetics of ^{11}C-ITMM in the cerebellar cortex. The rank order of V_T values corresponded well to the estimated mGluR1 density in the human brain. To estimate the binding potential of ^{11}C-ITMM, a reference tissue model may be useful for quantification of mGluR1 (*35,36*). The pons, a region with negligible mGluR1, may be used as an apparent reference region. However, the pons is located near the cerebellum, the region with the highest level of radioactivity in the brain, and hence radioactive signals in the cerebellum would spill into the pons. Alternatively, the striatum and occipital cortex (V_T = 0.61 ± 0.11; n = 5) could be used as apparent reference regions because of low uptake of ^{11}C-ITMM comparable to that in the pons. However, even at low levels, mGluR1 is present throughout the mammalian brain, especially in the basal ganglia (*9*). Moreover, ^{11}C-ITMM and the same pharmacophore ligand ^{18}F-FITM clearly showed a blocking effect in all brain regions of rodent and monkey, respectively (*19,22*). Therefore, it is not clear that a real reference region will be available, and hence further blocking studies using selective mGluR1 antagonists are needed.

A disadvantage of ^{11}C-ITMM is the low uptake in the moderate- or low-mGluR1 brain regions, such as the thalamus, hippocampus, and cerebral cortex. Therefore, the signal of ^{11}C-ITMM from regions outside the cerebellum would be difficult to assess, given their low physiologic uptake, possibly reducing the clinical applications of ^{11}C-ITMM in various neurologic and psychiatric disorders. In contrast, ^{11}C-ITMM may be useful to understand the mechanisms of pathogenesis and disease progression of cerebellar diseases, such as spinocerebellar ataxia. In patients with Hodgkin disease, autoantibodies against mGluR1 were shown to cause deficits in motor coordination and degeneration of Purkinje cells (*37*). Interestingly, blockade of mGluR1 expression in adult mGluR1 conditional knockout mice led to impaired motor coordination (*38*). The cerebellum is important for sensorimotor control and plays a crucial role in intra- and interlimb coordination. It would be of interest to determine whether there are alterations of mGluR1 in aged people with gait disturbances using PET with ^{11}C-ITMM.

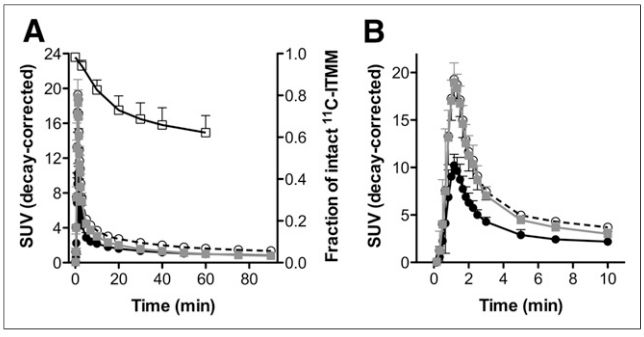

FIGURE 5. Mean decay-corrected time–activity curves of whole blood (●), plasma (○), metabolite-corrected plasma (■), and fraction of intact ^{11}C-ITMM (□) after intravenous injection of ^{11}C-ITMM into human subject. (A) Radioactivity levels of whole blood, plasma, and metabolite-corrected plasma are expressed as SUVs. (B) Values for 10 min were extracted from A. Considerably higher levels of radioactivity were observed in plasma fraction. Data represent mean ± SD of 5 subjects.

CONCLUSION

The initial findings of the present study in a small group of subjects indicated that ^{11}C-ITMM PET is feasible for imaging cerebellar mGluR1 with acceptable dosimetry and pharmacologic safety at the dose required for adequate PET imaging. The brain uptake of ^{11}C-ITMM can be calculated as V_T, which is an index of receptor density. The values of V_T for ^{11}C-ITMM were well identified and showed relatively small degrees of variation in this group of 5 healthy subjects.

DISCLOSURE

The costs of publication of this article were defrayed in part by the payment of page charges. Therefore, and solely to indicate this fact, this article is hereby marked "advertisement" in accordance with 18 USC section 1734. This work was supported by a Grant-in-Aid for Scientific Research (B) No. 24390298 from the Japan Society for the Promotion of Science. No other potential conflict of interest relevant to this article was reported.

ACKNOWLEDGMENTS

We thank Kunpei Hayashi and Hatsumi Endo for technical assistance.

REFERENCES

1. Schoepp DD. Unveiling the functions of presynaptic metabotropic glutamate receptors in the central nervous system. *J Pharmacol Exp Ther.* 2001;299:12–20.
2. Nakanishi S. Metabotropic glutamate receptors: synaptic transmission, modulation, and plasticity. *Neuron.* 1994;13:1031–1037.
3. Conn PJ, Pin JP. Pharmacology and functions of metabotropic glutamate receptors. *Annu Rev Pharmacol Toxicol.* 1997;37:205–237.
4. Knöpfel T, Grandes P. Metabotropic glutamate receptors in the cerebellum with a focus on their function in Purkinje cells. *Cerebellum.* 2002;1:19–26.
5. Smith Y, Charara A, Hanson JE, Paquet M, Levey AI. $GABA_B$ and group I metabotropic glutamate receptors in the striatopallidal complex in primates. *J Anat.* 2000;196:555–576.
6. Fotuhi M, Sharp AH, Glatt CE, et al. Differential localization of phosphoinositine-linked metabotropic glutamate receptor (mGluR1) and the inositol 1,4,5-trisphsophata receptor in rat brain. *J Neurosci.* 1993;13:2001–2012.
7. Lavreysen H, Pereira SN, Leysen JE, Langlois X, Lesage AS. Metabotropic glutamate 1 receptor distribution and occupancy in the rat brain: a quantitative autoradiographic study using [^{3}H]R214127. *Neuropharmacology.* 2004;46:609–619.
8. Steckler T, Oliveira AF, van Dyck C, et al. Metabotropic glutamate receptor 1 blockade impairs acquisition and retention in a spatial water maze task. *Behav Brain Res.* 2005;164:52–60.
9. Ferraguti F, Crepaldi L, Nicoletti F. Metabotropic glutamate 1 receptor: current concepts and perspective. *Pharmacol Rev.* 2008;60:536–581.
10. Swanson CJ, Bures M, Johnson MP, Linden AM, Monn JA, Schoepp DD. Metabotropic glutamate receptors as novel targets for anxiety and stress disorders. *Nat Rev Drug Discov.* 2005;4:131–144.
11. Ribeiro FM, Paquet M, Cregan SP, Ferguson SS. Group I metabotropic glutamate receptor signaling and its implication in neurological disease. *CNS Neurol Disord Drug Targets.* 2010;9:574–595.

12. Huang Y, Narendran R, Bischoff F, et al. A positron emission tomography radioligand for the in vivo labeling of metabotropic glutamate 1 receptor: (3-ethyl-2-[^{11}C]methyl-6-quinolinyl)(cis-4-methoxycyclohexyl)methanone. *J Med Chem.* 2005;48:5096–5099.
13. Yanamoto K, Konno F, Odawara C, et al. Radiosynthesis and evaluation of [^{11}C] YM-202074 as a PET ligand for imaging the metabotropic glutamate receptor type 1. *Nucl Med Biol.* 2010;37:615–624.
14. Prabhakaran J, Majo VJ, Milak MS, et al. Synthesis, in vitro and in vivo evaluation of [^{11}C]MMTP: a potential PET ligand for mGluR1 receptors. *Bioorg Med Chem Lett.* 2010;20:3499–3501.
15. Hostetler ED, Eng W, Joshi AD, et al. Synthesis, characterization, and monkey PET studies of [^{18}F]MK-1312, a PET tracer for quantification of mGluR1 receptor occupancy by MK-5435. *Synapse.* 2011;65:125–135.
16. Fujinaga M, Yamasaki T, Kawamura K, et al. Synthesis and evaluation of 6-[1-(2-[^{18}F]fluoro-3-pyridyl)-5-methyl-1*H*-1,2,3-triazol-4-yl]quinoline for positron emission tomography imaging of the metabotropic glutamate receptor type 1 in brain. *Bioorg Med Chem.* 2011;19:102–110.
17. Fujinaga M, Maeda J, Yui J, et al. Characterization of 1-(2-[^{18}F]fluoro-3-pyridyl)-4-(2-isopropyl-1-oxo-isoindoline-5-yl)-5-methyl-1*H*-1,2,3-triazole, a PET ligand for imaging the metabotropic glutamate receptor type 1 in rat and monkey brains. *J Neurochem.* 2012;121:115–124.
18. Yamasaki T, Fujinaga M, Yoshida Y, et al. Radiosynthesis and preliminary evaluation of 4-[^{18}F]fluoro-*N*-[4-[6-(isopropylamino)pyrimidin-4-yl]-1,3-thiazol-2-yl]-*N*-methylbenzamide as a new positron emission tomography ligand for metabotropic glutamate receptor subtype 1. *Bioorg Med Chem Lett.* 2011;21:2998–3001.
19. Yamasaki T, Fujinaga M, Maeda J, et al. Imaging of metabotropic glutamate receptor subtype 1 in rat and monkey brains using PET with [^{18}F]FITM. *Eur J Nucl Med Mol Imaging.* 2012;39:632–641.
20. Zanotti-Fregonara P, Barth VN, Liow JS, et al. Evaluation in vitro and in animals of a new ^{11}C-lableled PET radioligand for metabotropic glutamate receptors 1 in brain. *Eur J Nucl Med Mol Imaging.* 2013;40:245–253.
21. Mu L, Schubiger A, Ametamey SM. Radioligands for the PET imaging of metabotropic glutamate receptor subtype 5 (mGluR5). *Curr Top Med Chem.* 2010;10:1558–1568.
22. Fujinaga M, Yamasaki T, Yui J, et al. Synthesis and evaluation of novel radioligands for positron emission tomography imaging of metabotropic glutamate receptor subtype 1 (mGluR1) in rodent brain. *J Med Chem.* 2012;55:2342–2352.
23. Toyohara J, Sakata M, Fujinaga M, et al. Preclinical and the first clinical studies on [^{11}C]ITMM for mapping metabotropic glutamate receptor subtype 1 by positron emission tomography. *Nucl Med Biol.* 2013;40:214–220.
24. Lavreysen H, Wouters R, Bischoff F, et al. JNJ16259685, a highly potent, selective and systemically active mGlu1 receptor antagonist. *Neuropharmacology.* 2004;47:961–972.
25. Sakata M, Wu J, Toyohara J, et al. Biodistribution and radiation dosimetry of the α7 nicotinic acetylcholine receptor ligand [^{11}C]CHIBA-1001 in humans. *Nucl Med Biol.* 2011;38:443–448.
26. Fujiwara T, Watanuki S, Yamamoto S, et al. Performance evaluation of a large axial field-of-view PET scanner: SET-2400W. *Ann Nucl Med.* 1997;11:307–313.
27. Meikle SR, Bailey DL, Hooper PK, et al. Simultaneous emission and transmission measurements for attenuation correction in whole-body PET. *J Nucl Med.* 1995;36:1680–1688.
28. Kirschner AS, Ice RD, Beierwaltes WH. Radiation dosimetry of ^{131}I-19-iodocholesterol: the pitfalls of using tissue concentration data–Reply. *J Nucl Med.* 1975;16:248–249.
29. Stabin MG, Sparks RB, Crowe E. OLINDA/EXM: the second-generation personal computer software for internal dose assessment in nuclear medicine. *J Nucl Med.* 2005;46:1023–1027.
30. International Commission on Radiological Protection. *1990 Recommendation of the International Commission on Radiological Protection.* Publication 60. Oxford, U.K.: Pergamon Press; 1990.
31. Ashburner J. A fast diffeomorphic image registration algorithm. *Neuroimage.* 2007;38:95–113.
32. Zanotti-Fregonara P, Innis RB. Suggested pathway to assess radiation safety of ^{11}C-labeled PET tracers for first-in-human studies. *Eur J Nucl Med Mol Imaging.* 2012;39:544–547.
33. van der Aart J, Hallett WA, Rabiner EA, Passchier J, Comley RA. Radiation dose estimates for carbon-11-labelled PET tracers. *Nucl Med Biol.* 2012;39:305–314.
34. Logan J, Fowler JS, Volkow ND, et al. Graphical analysis of reversible radioligand binding from time-activity measurements applied to [*N*-^{11}C-methyl]-(−)-cocaine PET studies in human subjects. *J Cereb Blood Flow Metab.* 1990;10:740–747.
35. Gunn RN, Gunn SR, Cunningham VJ. Positron emission tomography compartmental models. *J Cereb Blood Flow Metab.* 2001;21:635–652.
36. Yaqub M, Tolboom N, Boellaard R, et al. Simplified parametric methods for [^{11}C]PIB studies. *Neuroimage.* 2008;42:76–86.
37. Coesmans M, Smitt PA, Linden DJ, et al. Mechanisms underlying cerebellar motor deficits due to mGluR1-autoantibodies. *Ann Neurol.* 2003;53:325–336.
38. Nakao H, Nakao K, Kano M, Aiba A. Metabotropic glutamate receptor subtype-1 is essential for motor coordination in the adult cerebellum. *Neurosci Res.* 2007;57:538–543.